

Original paper

Morphology and Raman spectral parameters of Bohemian microdiamonds: implications to elastic geothermobarometry

Petra JAKUBOVÁ^{1*}, Jana KOTKOVÁ^{1,2}, Richard WIRTH³, Radek ŠKODA¹, Jakub HAIFLER¹

¹ Department of Geological Sciences, Faculty of Science, Masaryk University, Kotlářská 267/2, 611 37 Brno, Czech Republic; petra.jakubova@centrum.cz

² Czech Geological Survey, Klárov 3, 118 21 Prague 1, Czech Republic

³ Interface Geochemistry, GFZ German Research Centre For Geosciences, Telegrafenberg, C-120, 14473 Potsdam, Germany

* Corresponding author



In this work, we combine the morphology and internal structure of northwestern Bohemian microdiamonds with their Raman spectral parameters to describe and understand their relationship. We evaluate our data according to the theory of elasticity and discuss implications for elastic geothermobarometry of diamond inclusions in garnet. We conclude that microdiamonds enclosed in kyanite, garnet and zircon differ in morphology and internal structure depending on the type of the host rock and host phase. Single crystal diamond octahedra in kyanite in the acidic gneiss show predominantly Raman shift towards higher wavenumbers (upshift), while single and polycrystalline diamonds enclosed in garnet and zircon in the intermediate garnet–clinopyroxene rock yield more variable Raman shift including a shift towards lower wavenumbers (downshift). This is consistent with closed boundaries between diamond and kyanite observed using FIB-TEM, while interfaces between diamond and garnet or zircon are commonly open. Moreover, higher variability in the Raman shift in diamond hosted by garnet or zircon may be caused by complex internal structure and the presence of other phases. At the same time, a diamond in kyanite features relatively high full-width-at-half-maximum (*FWHM*) due to the anisotropy of thermal contraction, which is reflected by the plastic deformation of diamond mediated by dislocation glide at $T \geq 1000$ °C. The entrapment pressure (P_{trap}) for diamonds in garnet was calculated using elastic geobarometry to test its compatibility with the existing peak pressure estimated by conventional thermobarometry. The “downshifted” diamonds exhibit entrapment pressures of 4.8 ± 0.14 and 4.99 ± 0.14 GPa at an entrapment temperature of 1100 °C, using unstrained reference diamond from the literature and own measurements, respectively. This is consistent with the earlier estimates and the elastic theory and does not require any elastic resetting suggested to account for the reported upshift in garnet. Our data suggest that the upshift in diamond hosted by garnet is related to the proximity of other diamond grains. We conclude that the use of diamond inclusions in elastic barometry should be backed by careful evaluation of its internal structure and associated phases and restricted to isometric monocrystalline diamond grains not occurring in clusters as required by the method.

Keywords: microdiamond, ultra-high-pressure rock, Raman spectroscopy, morphology, elastic geobarometry, Bohemian Massif

Received: 21 February 2022; accepted: 17 June 2022; handling editor: R. Skála

The online version of this article (doi: 10.3190/jgeosci.356) contains supplementary electronic material.

1. Introduction

Elastic geobarometry represents a complementary method to geothermobarometry and phase equilibria to constrain the pressure–temperature (P – T) conditions of the formation of minerals and rocks. It is based on measurements of residual pressure that develops in a mineral inclusion entrapped in a mineral host during any change in external PT conditions, namely cooling and exhumation (pressure release), due to their contrasting thermo–elastic properties such as thermal expansion and compressibility (Rosenfeld and Chase 1961; Parkinson and Katayama 1999; Enami et al. 2007). The residual pressure of the inclusion can be estimated based on its relative Raman shift compared to atmospheric pressure, using experimental or empiric calibrations relating the shift of the Raman band of the inclu-

sion from the unstrained reference to the inclusion pressure (e.g., Hanfland and Syassen 1985; Angel et al. 2018).

To calculate the entrapment pressure, various formulations of elastic solutions based on linear or non-linear elasticity have been proposed (see Moulas et al. 2020 and references therein). In these, spherical isotropic inclusions in an elastically isotropic host represent the simplest approximation. The quartz-in-garnet system represents such a case, as garnet is almost elastically isotropic, and quartz behavior can be approximated as isotropic as well (e.g., Bonazzi et al. 2019). Quartz-in-garnet geobarometry has been widely used because of its geological relevance and because quartz represents relatively soft inclusion in a relatively stiff host phase and thus develops overpressure during exhumation (e.g., Kohn 2014; Angel et al. 2015).

Inclusions of diamond in garnet represent an opposite situation when a stiff phase (diamond) is enclosed in a softer host (silicate). Nevertheless, some of these diamond inclusions also show residual pressure (e.g., Perraki et al. 2009; Korsakov et al. 2015; Nasdala et al. 2016). Angel et al. (2015) attributed this effect to elastic resetting of inclusion by plastic deformation of the host.

To address this problem, we focus on microdiamonds in ultrahigh-pressure–ultrahigh-temperature (UHP–UHT) metamorphic rocks overprinted under HP granulite-facies conditions from the northwestern part of the Bohemian Massif within the European Variscan orogenic belt (Kotková et al. 2011). These microdiamonds represent a unique material for evaluating the recorded under/overpressure and its controlling factors for several reasons. First, they are enclosed in garnet with cubic, high crystallographic symmetry which will therefore develop isotropic strain under hydrostatic stress (Mazzucchelli et al. 2019) as well as kyanite and zircon (elastically anisotropic). Second, they are well-preserved, without graphitization features, and they form individual grains in the host phases – unlike other microdiamonds in the world that can show graphite coatings and make part of the multiphase solid inclusions (see Kotková et al. 2021 and references therein). Third, they include both perfect octahedral crystals and imperfect cuboid forms. Fourth, the presence of diamonds in Ti-rich zircon domains (up to 190 ppm) allows constraining their entrapment at ≥ 1100 °C and 4.5–5.0 GPa, P – T conditions similar to those determined for the associated garnet peridotites (Medaris et al. 2015; Haifler and Kotková 2016). The rocks were exhumed along a near-to-isothermal (ITD) adiabatic exhumation path, characteristic of diamond-bearing ultrahigh-pressure terranes worldwide (Haifler and Kotková 2016; Kotková et al. 2021). U–Pb ages of zircon and rutile overlap close to 340 Ma, suggesting a rapid exhumation (Kotková et al. 1996).

In this work, we focus on morphology and Raman spectral parameters, i.e., Raman band shift and $FWHM$ of microdiamonds enclosed in different phases in a set of UHP crustal rocks. We examine the effect of diamond morphology, internal structure and diamond–host relationship on its stress state (recorded under/overpressure), and its relationship to the pressure of inclusion entrapment.

2. Samples and methods

2.1. Sample description

We examined microdiamonds 10–30 microns in size, enclosed in kyanite, garnet and zircon in two host rock types: acidic quartzofeldspathic gneiss and intermediate garnet–clinopyroxene rock with granulite-facies mineral assemblage garnet–kyanite–feldspar–quartz and garnet–clinopyroxene–feldspar–quartz, respectively. The samples originate from both drillcores from boreholes T7 and T38 at the village of Staré, reaching the Saxothuringian basement, and from outcrops in an abandoned quarry in Stráž nad Ohří in the Eger Crystalline Complex (Kotková 1993; Kotková et al. 2011, 2016; Haifler and Kotková 2016). Our set of samples involves one acidic gneiss (T7 drillcore) and three intermediate rocks – one from T38 drillcore and two from the Stráž nad Ohří quarry (Tab. 1).

Acidic gneiss from T7 drillcore contains porphyroblasts of garnet (up to 2 mm in size) and kyanite within the matrix formed by mesoperthite and quartz, and late biotite. Garnets are equant and kyanite does not show any undulous extinction. Apatite, zircon, rutile and graphite are accessory phases. Microdiamonds are enclosed mostly in kyanite (Figs 1a, b), rarely in garnet, and also in rare zircon. The microdiamonds from this rock are exclusively single crystal octahedra.

Garnet–clinopyroxene rock (sample 95, Stráž nad Ohří quarry) contains large, mostly equant garnet (1–3 mm in diameter), clinopyroxene, and rare kyanite in a heterogeneous matrix consisting of antiperthitic feldspar, individual plagioclase and K-feldspar, and quartz. Biotite is a late phase and rutile, apatite, zircon, graphite and pyrite are common accessory phases. Microdiamonds are cuboctahedra to cuboids mainly occurring in clusters in garnet (Fig. 1c) and zircon (Fig. 1d).

Intermediate sample St14 from Stráž nad Ohří quarry is very rich in garnet, which forms porphyroblasts (up to 2 mm in diameter) within quartzofeldspathic matrix. This rock is strongly retrogressed with voluminous amphibole and biotite developing at the expense of garnet and rarely preserved clinopyroxene. Diamonds are cuboids (based on microscopy) being preserved primarily as inclusions in zircon, less commonly in garnet (Fig. 1e).

Tab. 1 List of studied samples and localities

Sample No.	Locality	Rock type	Host phase	Diamond morphology	Sample character	Name in plots
T7	drillcore Staré	acidic	Ky	octahedron	thin section and separated grains	KY T7
95	outcrop: western part of a disused quarry in Stráž n. Ohří	intermediate	Grt, Zrn	cuboctahedron	Grt – thin section Zrn – separated grains	GRT 95 ZRN 95 GRT95 SURF ZRN 95 SURF
T38	drillcore Staré	intermediate	Grt	cuboctahedron	thin section	GRT T38
St14	outcrop: eastern part of a disused quarry in Stráž n. Ohří	intermediate	Zrn	cuboctahedron	separated grains	ZRN St14 ZRN St14 SURF

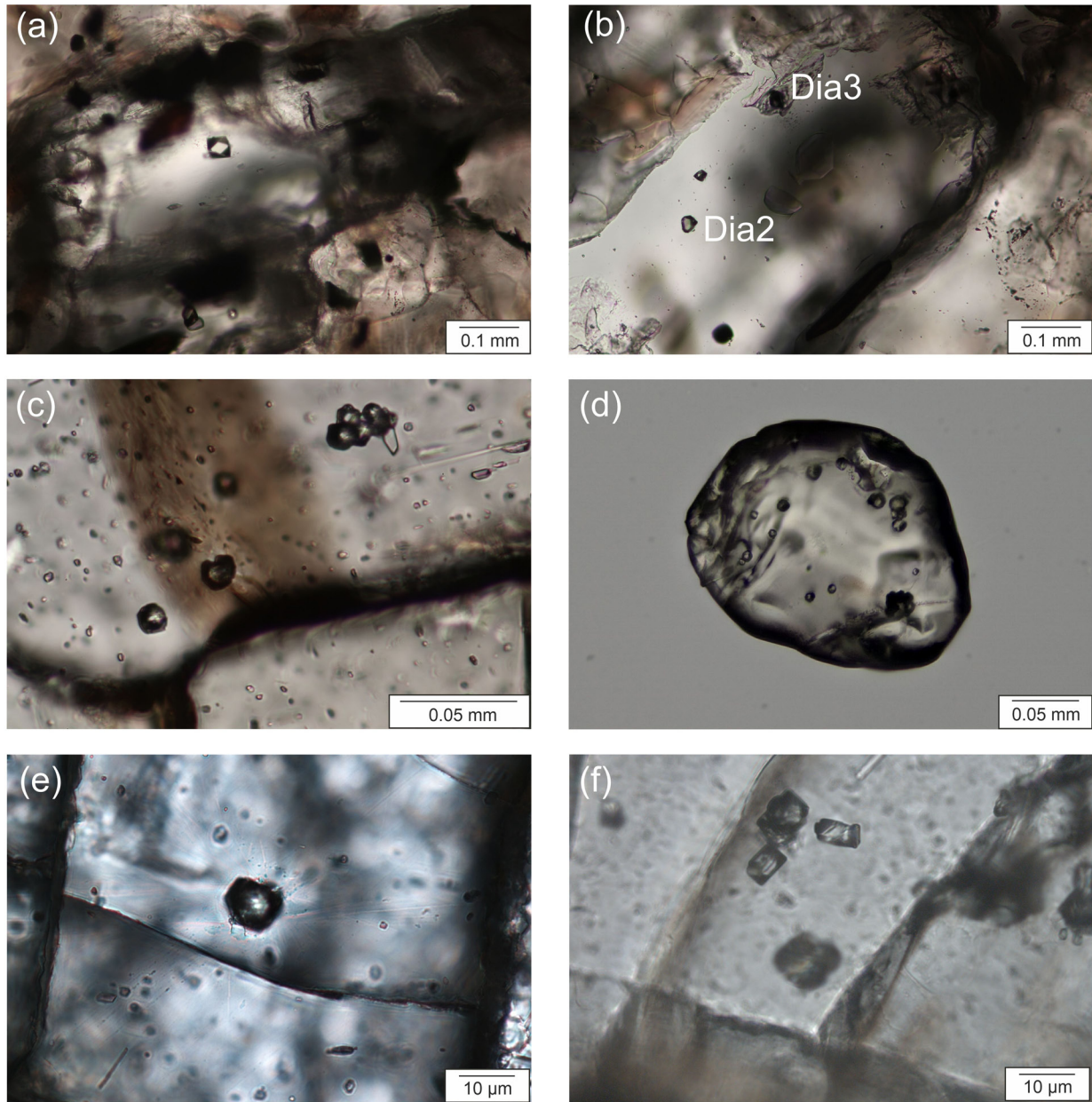


Fig. 1 – Photomicrographs of diamonds (Dia) enclosed in various host phases. **a–b** – diamond octahedra enclosed in kyanite (below and on the surface, respectively); Dia2 and Dia3 are shown in Figs 2a and b), acidic gneiss, T7 drillcore; **c–d** – diamond cuboids in garnet (c, below surface) and zircon (d), intermediate rock 95 outcrop; **e** – diamond cuboid in garnet (on the surface), intermediate rock St14 outcrop; **f** – diamond cuboids and rare elongated diamond enclosed at several levels of garnet host, intermediate rock, T38 drillcore. Mineral abbreviations according to Warr (2021).

The intermediate garnet–clinopyroxene rock sample from T38, depth 258 m, contains abundant large garnet porphyroblasts (up to 3mm in size) and smaller grains of clinopyroxene in a matrix dominated by plagioclase and quartz. Clinopyroxene is extensively replaced by amphibole, and some late biotite forming at the expense of garnet is also present. This sample is characterized by the presence of diamond clusters in garnet (Fig. 1f), dominated by cuboids, with an elongated diamond grain also present (based on optical microscopy; check Fig. 1f).

2.2. Methods

We studied polished rock sections of 30 and 300 μm thickness and epoxy mounts of separated host mineral grains. The samples were polished using Al_2O_3 abrasives to avoid contamination by synthetic diamond from polishing material and successively hand-polished using OP–U colloidal silica suspension of 0.04 μm grain size (Struers) so that the diamonds stand out above the surface of host minerals.

The samples were studied in transmitted and reflected light using an Olympus BX 41 optical microscope to identify micro-diamond inclusions in major silicates and zircon.

Scanning Electron Microscope (SEM) imaging has been carried out at Tescan Corp. in Brno. Uncoated diamond samples were imaged using a VEGA3 SEM (LaB₆ emitter), equipped with panchromatic cathodoluminescence (CL) detector and ultra-fast YAG scintillator back-scattered electron (BSE) detector in Low Vacuum mode (10 to 100 Pa) and in N₂ atmosphere. The gold-coated samples were imaged using a MIRA3 SEM (FEG Schottky source) equipped with YAG scintillator BSE and color CL detector. Accelerating voltage for both instruments ranged between 15 and 25 kV.

Raman spectra of diamonds were collected with a Horiba Labram HR Evolution spectrometer. This dispersive, edge-filter-based system is equipped with an Olympus BX 41 optical microscope, a diffraction grating with 1800 grooves per millimeter, and a Peltier-cooled, Si-based charge-coupled device (CCD) detector. The 532 nm Nd:YAG diode laser with a beam power of ~50 mW was selected for spectra acquisition. Raman signals of diamonds were collected in the range of 1100–1500 cm⁻¹ with a 100× objective (NA 0.9) and the system being operated in the confocal mode, beam diameter was ~0.8 μm, the axial resolution ~3–4 μm and power at the sample surface ~5 mW. No visual damage to the analyzed surface was observed under these conditions after the excitation. Wavenumber calibration was done using the Rayleigh line and low-pressure Ne-discharge lamp emissions at 571.923 and 574.830 nm (Supplementary data, ESM1), which are located close to the main diamond band at ~1332 cm⁻¹. The spectral resolution was ~0.5 cm⁻¹. The effect of the instrumental drift during the whole-day analytical session in the air-conditioned laboratory with a stable temperature of 21 ± 1 °C was negligible (ESM1). The Raman mapping was conducted using a 1 μm step grid and the same experimental setting. The spectra of associated phases were collected in the range of 100–4000 cm⁻¹ in a mode of spot analysis. The Raman spectra of the host zircon were also acquired to exclude its metamictization. All the Raman shifts are within fitting error of 0.01 cm⁻¹. For elastic geobarometry, cores of diamonds that were sufficiently isolated (at least three times their radius, Mazzucchelli et al. 2018) concerning the distance from the surface and bottom of the prepartate and, where possible, to the other inclusions (see Discussion), were analyzed. The spectral parameters of diamonds have been evaluated in relation to the published Raman spectrum of the well-crystalline macroscopic diamond at room temperature, characterized by the main Raman band at ~1331.8 ± 0.2 cm⁻¹ and an *FWHM* of ~1.65 ± 0.02 cm⁻¹ (Krishnamurti 1954; Solin and Ramdas 1970; Knight and

White 1989). In addition, an unstrained diamond standard was measured during the experimental day with a stable main Raman band position at ~1332.0 ± 0.03 cm⁻¹.

Band fitting was done after appropriate background correction, assuming Voigt function, i.e., convolution of the Lorentzian and Gaussian functions for the shapes of individual bands (*PeakFit*; Jandel Scientific Software). The equation of Vácz (2014) was applied for an instrumental broadening.

Electron transparent foils for transmission electron microscopy (TEM) were prepared from pre-selected areas of interest by applying the site-specific focused-ion-beam (FIB) technique. The TEM foils had 15–20 μm width, 10–15 μm depth and approximately 150 nm thickness. An FEI Tecnai™ G2 F20 X-Twin transmission electron microscope (TEM) at GeoForschungs Zentrum (GFZ) in Potsdam, operating at 200 kV with a field emission gun (FEG) electron source, was used for analytical transmission electron microscopy (ATEM). The TEM instrument is equipped with a Gatan imaging filter (GIF Tridiem), allowing for energy-filtered imaging. ATEM was performed with an EDAX X-ray analyzer equipped with an ultra-thin window. The X-ray intensities were measured in scanning transmission mode (STEM), where the electron beam was scanned over a pre-selected area, minimizing mass loss during data acquisition. Details of the technique are given in Wirth (2004) and Wirth et al. (2009).

3. Results

3.1. Diamond morphology

SEM imaging has shown that diamonds are hosted chiefly by kyanite, less commonly by garnet and zircon, in the acidic gneiss. The diamonds show approximately the ideal octahedron with eight equally sized triangular faces, sharp edges and corners. Some crystals have slightly distorted habits with additional faces, e.g., (100) and (110) instead of pointed corners (Figs 2a, b), and they can even be elongated. The octahedral faces are smooth, flat with straight edges, in some cases with step-faces due to the development of numerous terraces formed by triangular growth plates (Fig. 2a). Dissolution features are rare and limited to a few single negative trigons on octahedral faces (Kotková et al. 2021). Octahedral macles also rarely occur (Fig. 2c).

Diamonds hosted by garnet and zircon in the intermediate rock 95 have different and more variable morphology than those from the acidic rock. Their typical crystal form is euhedral to subhedral cuboctahedron (cuboid), with sharp or sub-rounded edges and corners. The cuboctahedra show an almost equal proportion of (100) and (111) faces (Figs 2d, e, j, k), or octahedral

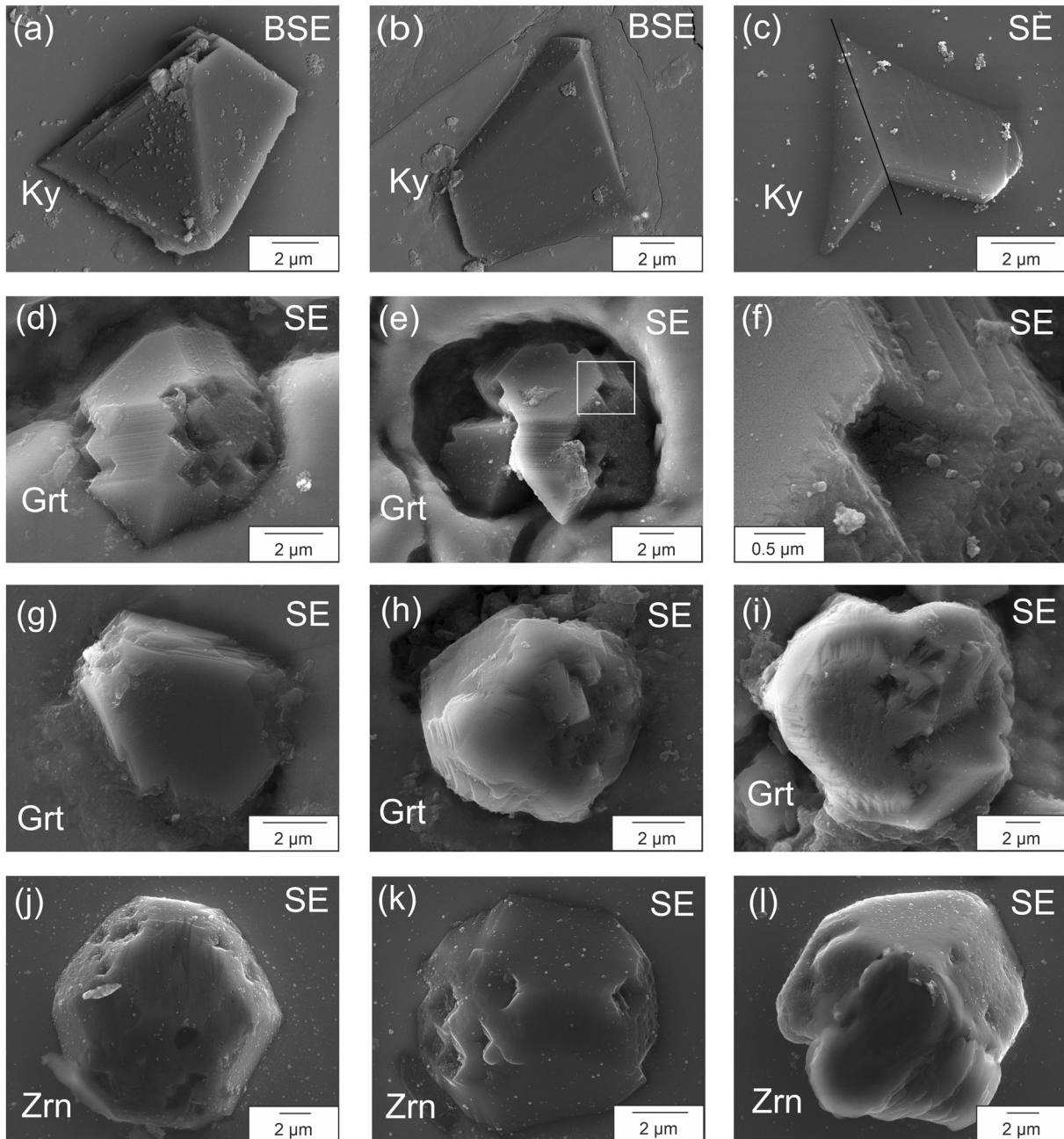


Fig. 2 – BSE and SE images of diamonds from the two UHP rock types. **a–c** – diamond octahedra enclosed in kyanite (Ky) in the acidic gneiss, T7 drillcore: **a, b** (Dia2 and Dia3 in Fig. 1 b) – slightly distorted octahedra with smooth faces and additional faces instead of pointed corners, with growth steps (**a**), **c** – diamond twin with a dark line indicating the twin plane. **d–i** – cubo-octahedral diamonds enclosed in garnet (Grt), intermediate rock, 95 outcrop: **d–f** – diamonds with equally sized face (**f** – detail of a tetragonal pit marked in **e**), **g** – diamond with predominant octahedral faces, **j–l** – cubo-octahedral diamonds enclosed in zircon (Zrn), intermediate rock 95 outcrop; **j–k** – diamonds with equal faces; **l** – rare macle. Four-digit number in the image **h** refers to the number of TEM foil. Figs **h, j** modified from Kotková et al. (2021).

faces predominate (Fig. 2g). While octahedral faces are smooth, the cubic ones are rough, with tetragonal pits concentrated at the corners and edges rather than within the cubic planes themselves (Figs 2d–f, h–l). Similar to the octahedral diamonds above, the octahedral layers show step faces at their surfaces, formed by individual growth planes with triangular (Fig. 2g) or, more com-

monly, hexagonal (octahedral with apices truncated by cube planes) shapes (Figs 2d, e, h). Their development results in the formation of additional “dodecahedral” (101), (011) and (110) faces with subparallel striations/steps (Figs 2d–f). This crystal form can be classified as a double truncated octahedron. Some grains are anhedral (Fig. 2i), and rare macles also occur (Fig. 2l).

3.2. Diamond – host relationships and diamond internal structure

FIB-TEM study has shown that the diamond octahedra enclosed in kyanite are regular idiomorphic crystals (Figs 3a, b). The phase boundary between diamond and kyanite host is straight and closed, without any associated phases or pore spaces except from a sub-micron layer of graphite and a low-pressure assemblage of ferrite, quartz and white mica, and a single cavity with relics of a quench phase (Fig. 3b, see also Kotková et al. 2021). The grains are homogeneous, without any core-rim structures in CL, or subgrains in FIB-TEM, and lack inclusions in their interior. Some diamonds are devoid of any defects, while others show abundant deformational features represented by straight and curved dislocation lines and low-angle grain boundaries (Fig. 3c). The curved dislocations, together with the low-angle grain boundaries, suggest a period of annealing after deformation where the dislocations started moving by diffusion processes and finally arranged in low-angle grain boundaries, thus reducing the internal energy of the diamond.

Cuboctahedral diamonds enclosed in garnet and zircon are in single crystals (Fig. 3d), or they are polycrystalline (2 of 6 grains studied by TEM, their presence on the surface of sample 95 is also confirmed by visible polishing scratches), being composed of numerous small diamond grains (Figs 3f, g, j). The polycrystalline grain shown in Fig. 3f is associated with micrometer-sized rutile and quartz, which is located on the uneven polycrystalline diamond surface, thus forming apparent inclusions (Fig. 3g). Nevertheless, also monocrystalline cuboids commonly have an irregular surface (Figs 2h, 3d). The interface between diamond and host garnet and zircon is straight, with steps (Fig. 3d), or curved, and it can be closed or partially opened, with elongated gaps and steps with (111) orientation creating a zig-zag surface (Figs 3h, i) containing amorphous quench material (see also Kotková et al. 2021). In addition, a 0.5 to 1 μm thick layer of graphite and amorphous carbon, with a straight boundary with diamond not indicating any replacement, occurs at the diamond interface with garnet (Fig. 3d) and zircon (Fig. 3k). There are no inclusions in the interior of the diamond except from a quench phase along some subgrain boundaries (see also Kotková et al. 2021). Diamond cuboctahedra contain fewer defects compared to the octahedra enclosed in kyanite. Diamonds hosted by zircon are devoid of dislocations, and those enclosed by garnet have only a few defects: a single low-angle grain boundary and dislocations radiating from a pore/cavity arranging to form a low-angle grain boundary (Figs 3d, e) were observed. CL imaging has shown that one cuboid diamond grain contains an octahedral-shaped dark core surrounded by a CL-bright rim (Fig. 3l).

The presence of associated phases (apatite, carbonate, quartz, or graphite) has also been demonstrated by the micro-Raman study in the case of diamonds enclosed in garnet in the sample T38.

3.3. Raman spectroscopy

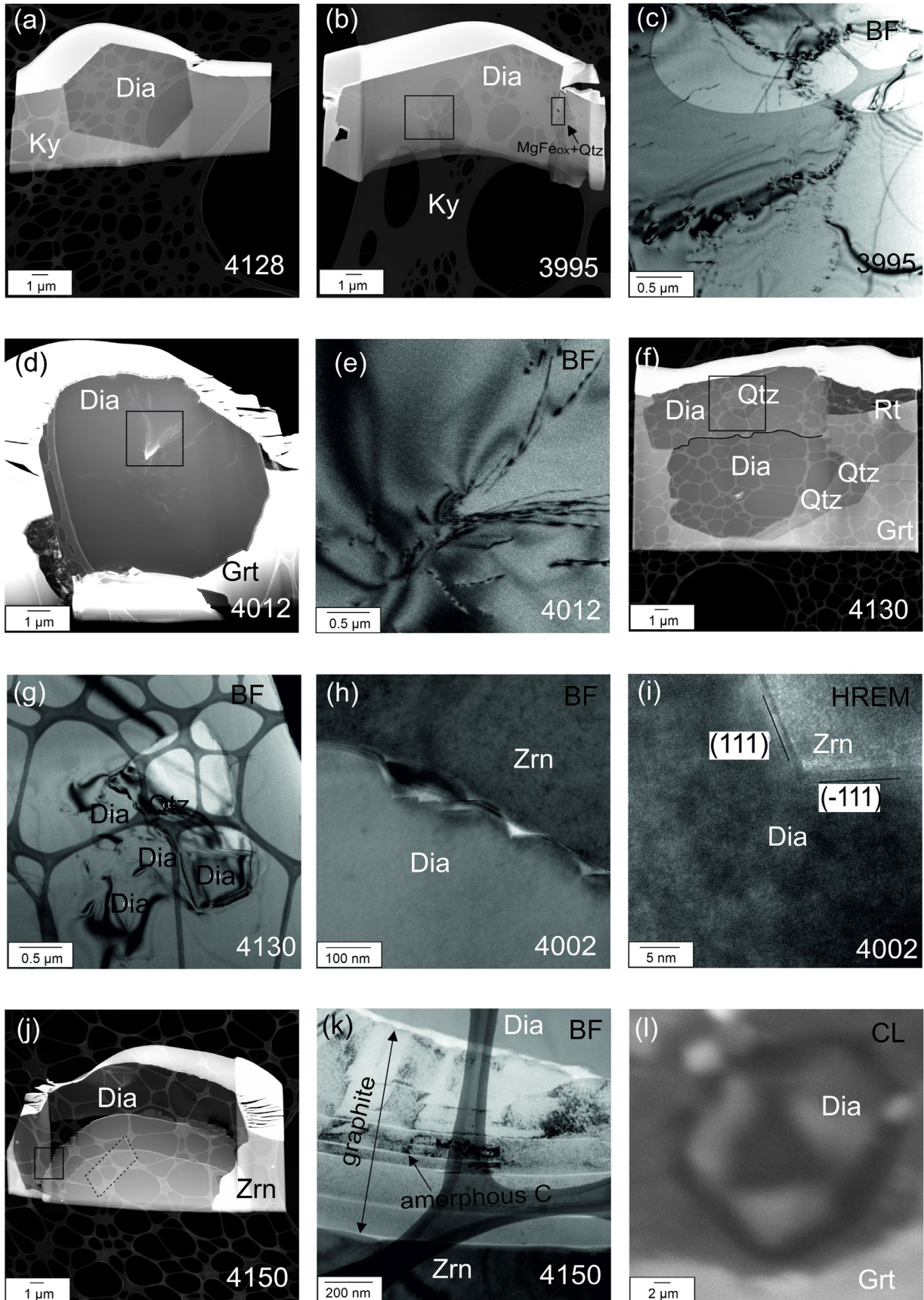
We measured Raman spectra, i.e., Raman shift and *FWHM*, of a large number (>100) of microdiamond grains enclosed in kyanite, garnet and zircon within the thin sections as well as in separated mineral grains in mounts (see Tab. 1). We mostly focused on the diamonds whose morphology, diamond-host relationships and internal structure were studied using SEM and FIB-TEM. In addition, Raman data were acquired for diamonds within a single garnet in a rare sample of intermediate garnet-clinopyroxene rock from T38 borehole and diamonds hosted by zircon in sample St14 from an outcrop. The cores of diamond grains, occurring both underneath and on the surface of the sample, were analyzed, the latter labeled SURF, and evaluated separately. The text below refers to the diamonds underneath the surface when not explicitly specified. In diamond grains with a large Raman upshift, its homogenous distribution was tested by more analyses, and a representative value from the measured shifts is presented.

The data are summarized and presented in Fig. 4 and in Supplementary data (ESM2). The investigated diamonds fall both in the upshift and downshift field, and the *FWHM* are broadened.

The position of the first-order Raman band of single diamond octahedra enclosed in kyanite in the acidic sample (drillcore T7) ranges between 1331.5 cm^{-1} and 1333.6 cm^{-1} , plotting predominantly in the up-shift region in

⇒

Fig. 3 – FIB-TEM (a–k) and CL images (l) of diamonds (Dia). **a–c** – diamond octahedra enclosed in kyanite (Ky), acidic gneiss, T7 drillcore: perfect octahedra with straight and closed interface with host kyanite (a, b), showing dislocation lines in their interior (b, detail in c – BF image); **d–g** – diamonds enclosed in garnet (Grt), intermediate rock, 95 outcrop: single cuboctahedron with irregular surface (d, see Fig. 2 h), radially arranged dislocations at a pore/cavity visible as dark contrast (d, detail in e – BF image) and a layer of late graphite; polycrystalline diamond cuboid and associated rutile (Rt) and quartz (Qtz) (verified using FFT HREM) on its uneven surface (f, detail in g – BF image). **h–k** – diamonds enclosed in zircon (Zrn), intermediate rock, 95 outcrop: h–i – BF resp. HREM image of a zig-zag diamond surface made of (111) growth planes, j – polycrystalline diamond (subgrain marked by dashed line) with curved surface and a layer of graphite and amorphous carbon at interface with zircon (solid line), k – a detail of the graphite layer and amorphous carbon (C); **l** – CL image of cuboid diamond, intermediate rock, T38 drillcore. Four-digit numbers refer to FIB-TEM sample numbers. BF – bright field, HREM – high-resolution electron microscopy, CL – cathodoluminescence. Figs a, b, d, f and j are high-angle annular dark field images (HAADF). The dark network in figures g and k represent the perforated carbon film the FIB foil is resting on. Figs b, f modified from Kotková et al. (2021).



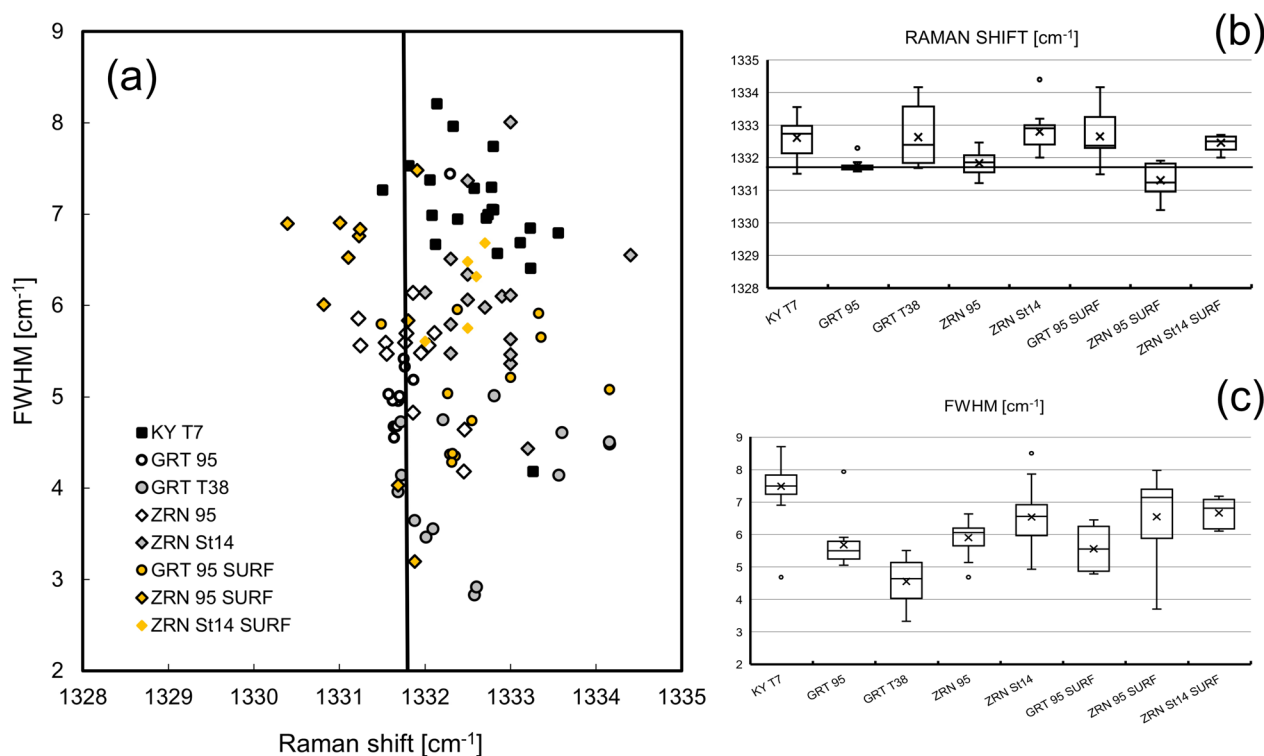


Fig. 4 – Raman data of microdiamonds in this study enclosed in kyanite, garnet and zircon distinguished by different rock types (acidic and intermediate UHP rocks) and by occurrence below or on the surface of its host phase. Zrn – zircon, Ky – kyanite, Grt – garnet, SURF – diamonds on the surface of a sample. See details in Tab.1: T7 acidic gneiss, drillcore. T38 intermediate rock, drillcore. 95, St14 intermediate rock, outcrop. **a** – plot of Raman shift against *FWHM*; **b**, **c** – box plots of the Raman band shift and *FWHM*, respectively. Lines show characteristic parameters of perfectly crystallized diamond (e.g. Krishnamurti 1954).

Figs 4a, b. The *FWHM* parameter mostly shows a narrow range of 6.4–8.2 cm⁻¹ (Figs 4a, c). The Raman spectral parameters do not vary with diamond morphology (i.e., perfect octahedra vs. elongated, distorted grains).

Cuboid diamonds in garnet and zircon in the intermediate samples yield a slightly more variable Raman shift of 1331.2–1334.4 cm⁻¹ compared to the diamond octahedra above, which falls both in the up- and down-shift region in Fig. 4a. The *FWHM* range (2.8–8.0 cm⁻¹) is also larger, with the lowest *FWHM* in diamond enclosed in garnet (especially GRT T38) compared to those enclosed in zircon. It needs to be noted that spectral parameters of diamonds in garnet and zircon in sample 95 are similar. As for diamonds in zircon, ZRN 95 shows relatively low Raman shift values compared to ZRN St14 at a similar *FWHM* range.

The Raman shift of the diamonds exposed on the surface is either lower (ZRN 95 and ZRN St14) or higher (GRT 95) compared to those underneath the surface. In sample GRT 95, the median of *FWHM* values of diamonds on and underneath the surface is similar despite the variable Raman shift. SEM and TEM data show that GRT 95 SURF diamonds are imperfect cuboctahedra or disintegrated grains, in some cases associated with graphite (ESM2). One diamond with a slight upshift is

polycrystalline. The diamond with extreme Raman shift values of 1334.1 cm⁻¹ is a strongly disintegrated grain with numerous sharp edges.

Diamonds ZRN 95 SURF are slightly downshifted from the characteristic diamond Raman band (1331.8 ± 0.2 cm⁻¹). SEM and TEM data for other diamonds hosted by zircon in sample 95 consistently show that these are either polycrystalline or imperfect octahedra with gaps or cavities at the interface. Moreover, a relatively thick layer of graphite and amorphous carbon has been observed (Figs 3j, k). In addition to graphite closely associated with diamond, separate graphite grains not related to diamond occur in host minerals.

Multiple measurements within several grains of diamonds revealed variations of the Raman band shift up to 0.8 cm⁻¹. To examine these variations in detail, two Raman maps were produced for diamond grains showing upshift (Figs 5a–d). Variations of Raman band positions in the octahedral grain KY T7 (Fig. 5a, b) are small and non-systematic (1333.4–1334.4 cm⁻¹), while the bandwidth is narrower in its outer part (3.3–4.4 cm⁻¹) compared to the center (4.4–5.2 cm⁻¹). Similarly, an elongated diamond in garnet (GRT T38) shows minor non-systematic variations of Raman band positions (1333.7–1334.4 cm⁻¹). By contrast, the *FWHM* of the

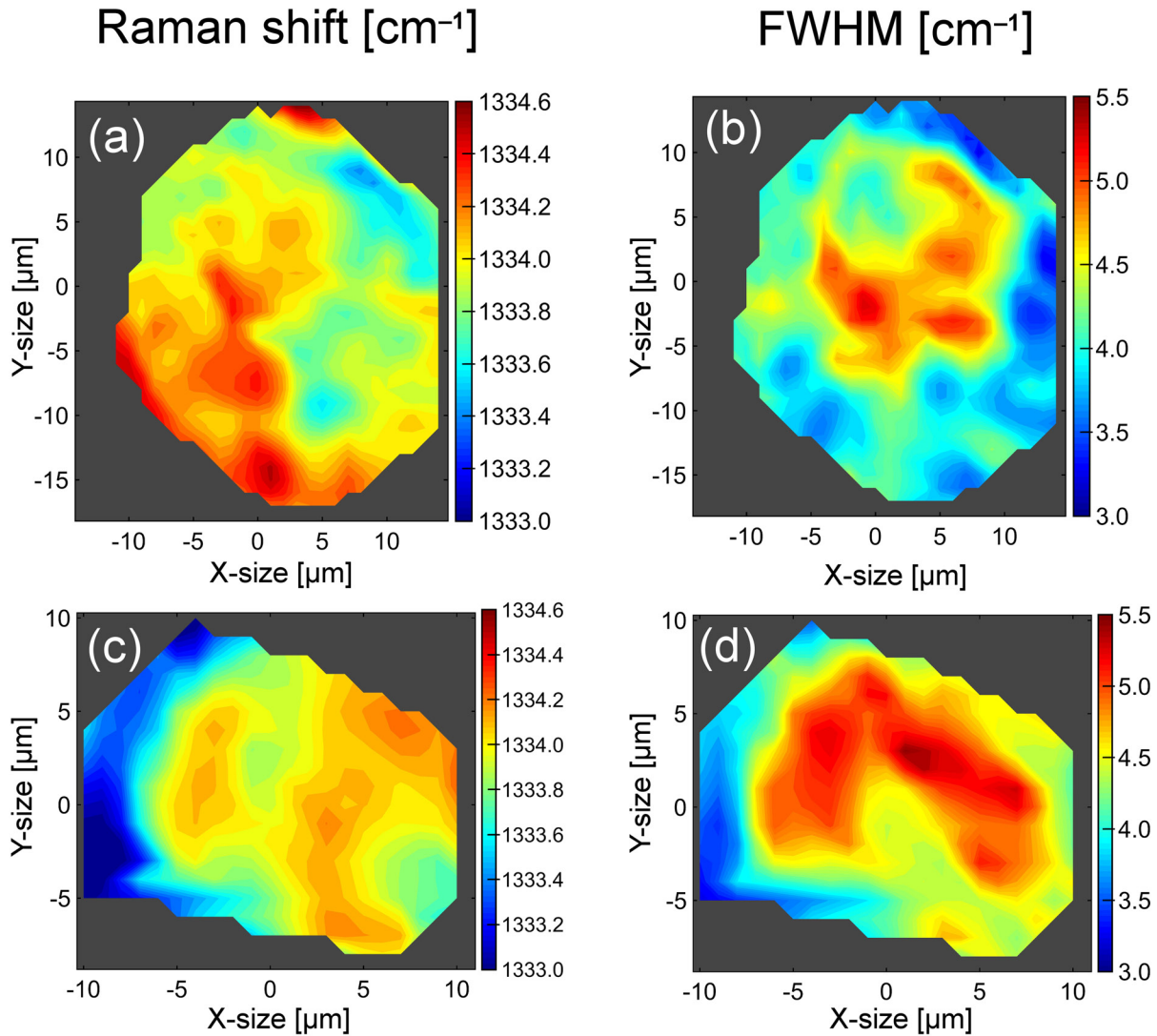


Fig. 5 – Raman maps of Raman shift and *FWHM* of diamonds. **a–b** – octahedron in kyanite, acidic gneiss, T7 drillcore; **c–d** – elongated diamond in garnet, intermediate rock, T38 drillcore.

band is narrower ($4.0\text{--}4.5\text{ cm}^{-1}$) in the mantle and rim area compared to the core ($4.5\text{--}5.5\text{ cm}^{-1}$). This grain overlaps with another cuboid grain visible in Fig. 5c, d with a nearly unshifted ($1333.0\text{--}1333.5\text{ cm}^{-1}$) and slightly broadened width ($3.0\text{--}3.8\text{ cm}^{-1}$) of a Raman band.

4. Discussion

For several reasons, we discuss our data within the context of microdiamond occurrences in the Kokchetav Massif, Kazakhstan, and the German Erzgebirge, because a) these are two best-studied areas represent UHP–UHT terranes, like the northwestern Bohemia, and b) garnet–phengite gneiss from the Erzgebirge and garnet–biotite gneisses from Kumdy-Kol in Kokchetav Massif are metasediments, which also applies for our samples (Kotková et al. 2021).

4.1. Diamond morphology and interpretation of distinct forms

4.1.1. Diamond morphology and mode of occurrence

Microdiamonds from northwestern Bohemia are hosted by kyanite, garnet and zircon, which is typical also for the other UHP–UHT rocks worldwide. The intermediate garnet–clinopyroxene rock contains cuboctahedra to cuboids, representing the major diamond morphology in the other UHP–UHT terranes (e.g., Shatsky et al. 1998; Korsakov et al. 2005; Dobrzhinetskaya et al. 2012, 2013; Kotková et al. 2021 and references therein). The predominance of octahedral diamonds in the acidic gneiss, by contrast, is a unique feature, only observed in non-retrogressed clinzoisite gneiss from Barchi Kol in the Kokchetav Massif. These diamonds show both smooth and rough surfaces

and stepped surfaces (De Corte et al. 2000; Korsakov et al. 2002; Ogasawara 2005; Perraki et al. 2009).

Crucial for our study is that diamonds from northwestern Bohemia are directly enclosed in their host, without any or with an insignificant number of other phases, including graphite. This, along with the mostly monocrystalline nature of the diamonds, allows evaluating host-inclusion relationships relevant to elastic geobarometry. By contrast, diamonds in the garnet–phengite gneiss from the Erzgebirge and garnet–biotite gneisses from the Kokchetav Massif commonly occur in multiphase solid inclusions along with quartz, feldspar, and micas, and both diamond cuboctahedra and octahedra (garnet–clinzoisite gneiss) are commonly associated with graphite (De Corte 2000; Dobrzhinetskaya et al. 2001, 2003, 2013; Stöckhert et al. 2001, 2009, Perraki et al. 2009; Korsakov et al. 2010; Zhang et al. 2017).

4.1.2. Relationship and significance of various microdiamond forms

In contrast to the simple octahedra from the acidic rock, the diamonds from the intermediate rock (Tab. 1) have complex morphology. The common form is a double truncated octahedron, representing a crystal form observed in nature (e.g., Fig. No 282 of Goldschmidt 1916) and diamond nanoparticles in material sciences (e.g., Barnard 2013).

Some microdiamond crystals in UHP–UHT terranes are rose-shaped aggregates of thin diamond plates with hexagonal shapes (Dobrzhinetskaya et al. 2001, 2003, 2007). However, our diamonds show the same orientation of these plates (Figs 2e, g, h). Moreover, our TEM data show that this external morphology does not propagate inside the crystal, which is homogeneous (Fig. 3d). This implies that these represent rather individual growth layers, i.e. (111) planes, than later grown plates on any pre-existing cuboid surface (c.f. Dobrzhinetskaya et al. 2001).

The nanoscale (111) planes observed at the diamond–zircon and diamond–garnet interface (Figs 3h, i) are interpreted as a growth feature due to the absence of any associated dislocations, which would be indicative of dissolution. These planes represent the growth steps at the margin of the octahedral planes.

It is known that crystal form depends on the supersaturation of the diamond-forming medium, expressed as a driving force, and the growth rate, with increasing parameters promoting the growth of cube forms and polycrystalline diamonds (Sunagawa 2005). The perfect crystal shape of octahedral diamonds, and the absence of inclusions in their interior, reflect a slow growth at equilibrium conditions, with the crystallization front migrating slowly without incorporating inclusions. This is conditioned by efficient diffusion supplying carbon to the growing crystal, requiring a higher temperature and/

or higher water content in the diamond-forming medium (see Kotková et al. 2021 and references therein). By contrast, the formation of cuboctahedra (cuboids), including polycrystalline diamonds, reflects a lower formation temperature when slow diffusion promotes the formation of many nucleation sites, i.e., high supersaturation and high nucleation rate (Sunagawa 2005). Apart from the temperature, water activity changes, which are linked to phase transitions from aqueous fluid to hydrous melt, trigger diamond crystallization, and control diamond characteristics (Kotková et al. 2021).

The terraces on the smooth octahedral faces of diamonds reflect two-dimensional nucleation, or layer-by-layer, growth, for both octahedral and cuboctahedral diamonds in both rock types. This growth mechanism requires a higher driving force characteristic of growth from a solution/melt (see, e.g., Sunagawa 2005; Woodruff 2015). Nevertheless, the similar growth mechanism and lack of inclusions suggest that the difference in supersaturation between the two crystal forms could be relatively small. This would provide an explanation for the common occurrence of both crystal forms in some UHP diamond-bearing terranes (Dobrzhinetskaya 2012; Kotková et al. 2021). Interestingly, the polycrystalline diamond from our study associated with quartz and rutile (Figs 3f, g) has an irregular surface and consists of randomly oriented nano-crystals, which are characteristic features of carbonado, experimentally produced at the lowest temperatures (e.g., Bovenkerk 1961).

Octahedron is the most common growth form of cratonic (kimberlitic) diamonds (Gurney et al. 2004). The presence of a triangular CL-dark core in one diamond cuboid within garnet (Fig. 3l) and growth steps on octahedral planes observed under SEM (Fig. 2g) suggest that the octahedron represents an initial growth form of cuboctahedra in the intermediate rock as well. The rapid growth of these octahedral planes resulted in their diminishing size, with the development of additional faces formed by traces of these planes and the increasing importance of the cube planes (e.g., Chernov 1974). In line with experimental works and the interpretations above, we suggest that evolution from octahedra to cuboctahedra reflects cooling (e.g., Bovenkerk 1961) rather than increasing supersaturation of the crystallizing medium. Our data are not consistent with the model of Shatsky et al. (1998) of the initial growth of cuboids, and octahedra, from a cube crystal because of decreasing supersaturation.

Our study provides some constraints on the discussion on the formation of diamond dodecahedra by growth in contrast to dissolution (Yamaoka et al. 1977; Sunagawa 2005 and references therein). While we observe the formation of dodecahedral faces (101), (011) and (110) as a result of the growth of octahedral planes, the final crystal

shape also includes the cube (100) planes, possibly due to cooling, as argued above. Interestingly, the formation of dodecahedra in experiments happens at relatively higher temperatures where octahedral and cubooctahedral diamond form, and close to the diamond-graphite transition and conditions of diamond dissolution (Yamaoka et al. 1977).

4.2. Raman spectral parameters of diamond inclusions

Our Raman data enable us to compare diamonds in various host phases and rock types within a single UHPM terrane. Microdiamonds from the northwestern Bohemia show the position of the first-order Raman band between 1331.2 cm^{-1} and 1334.4 cm^{-1} and *FWHM* ranging between 2.8 cm^{-1} and 8.2 cm^{-1} . There is a distinct difference between the higher Raman shift in diamond from KY T7 and the lower one of diamonds in GRT 95 and ZRN 95. The *FWHM* values of the perfect smooth octahedra in elastically anisotropic kyanite are relatively higher. However, the range of the Raman shift and *FWHM* is narrower than the imperfect cuboids enclosed both in cubic elastically quasi-isotropic garnet (Gonzalez et al. 2021) and elastically anisotropic zircon. While diamond cuboids in garnet feature the smallest *FWHM*, the *FWHM* of cuboids in zircon lies between that of garnet and kyanite. Diamonds from those samples where morphology and diamond-host relationships have been studied, diamonds ZRN 95 and ZRN 95 SURF, and diamonds KY T7 show a broad negative correlation between the Raman shift and *FWHM*.

4.2.1. Summary of Raman parameter variation in different diamond hosts

The variations of the Raman parameters of the studied diamonds are summarized based on diamond morphology, associated phases and internal diamond deformation from SEM and FIB-TEM analyses. This combined dataset demonstrates the following:

1. Perfect monocrystalline octahedra enclosed in kyanite show mostly the upshift of the Raman band and the highest *FWHM* in the dataset. At the same time, these strained diamonds show straight, closed boundaries with the host kyanite and internal deformational features. The presence of straight dislocation lines reflects the plastic behavior of diamond accomplished by dislocation glide. According to Yu et al. (2012) this develops due to anisotropic thermal contraction of kyanite upon cooling but at a still high enough temperature of $\sim 1000\text{ }^{\circ}\text{C}$.
2. Monocrystalline and polycrystalline cubooctahedra enclosed in garnet and zircon are located mostly in the downshift domain (slight upshift in the case of some diamonds in zircon; Fig. 4b). The lack of strain

in diamonds is consistent with the commonly observed gaps between diamond and host and the absence of internal deformation of the diamonds. Diamond in zircon shows a higher *FWHM* than garnet (Fig. 4c). Other features of the diamonds include their polycrystalline character and/or presence of the growth plates, and diamond association with minor amounts of other phases such as quartz and rutile.

3. Diamonds in garnet in sample T38, part of a cluster of diamond grains, represent an exception from the statement above, as it plots in the upshift domain. It also shows the largest Raman shift spread and the lowest *FWHM* (Fig. 4). Interestingly, the upshift was also identified in the diamonds on the surface of garnet (GRT 95 SURF) and in zircon (ZRN St14 and ZRN St14 SURF). This seems to contrast with the observed gaps between diamond and its host and the presence of late graphite.

4.2.2. Comparison with existing Raman data for microdiamonds

We compare our data with those of diamond inclusions in various host minerals from other UHP terranes (Fig. 6). However, the existing data do not always provide information on diamond morphology or coexisting phases, and host phases are not always distinguished. Moreover, data for diamond hosted by kyanite are extremely rare. Therefore, we only focus on the Raman shift data, as the *FWHM* values from different instruments are not directly comparable without a mathematical correction (Nasdala et al. 2016). The individual authors whose data are presented in Fig. 6 used either neon bands or an unstrained diamond to calibrate the Raman system except from Schmidt et al. (2010) and Zhang et al. (2017), where this information is not given. The Raman shift for diamond hosted by garnet in UHP–UHT terranes (Kokchetav Massif, Erzgebirge) is comparable to our data. Our diamonds show the highest Raman shift of 1334.4 cm^{-1} for diamond cuboids enclosed in garnet. The upshift of the Raman band is characteristic of many cuboidal diamond inclusions, namely in garnet both from the Kokchetav Massif and the Erzgebirge. An upshift was reported both for single diamond inclusions and diamonds (cuboids) within polyphase melt inclusions (e.g., Perraki et al. 2009; Nasdala et al. 2016), and for single diamond cuboids enclosed in garnet in garnet-clinopyroxene rocks (extreme values of 1338 cm^{-1} , see below) and octahedral diamond in garnet from garnet-clinozoisite rock (Korsakov et al. 2015).

By contrast, some diamonds show a significant downshift of the Raman band. This has been reported for diamonds enclosed by zircon from the Erzgebirge garnet–phengite gneiss (Zhang et al. 2017). These diamonds are described as polycrystalline or aggregated, and they

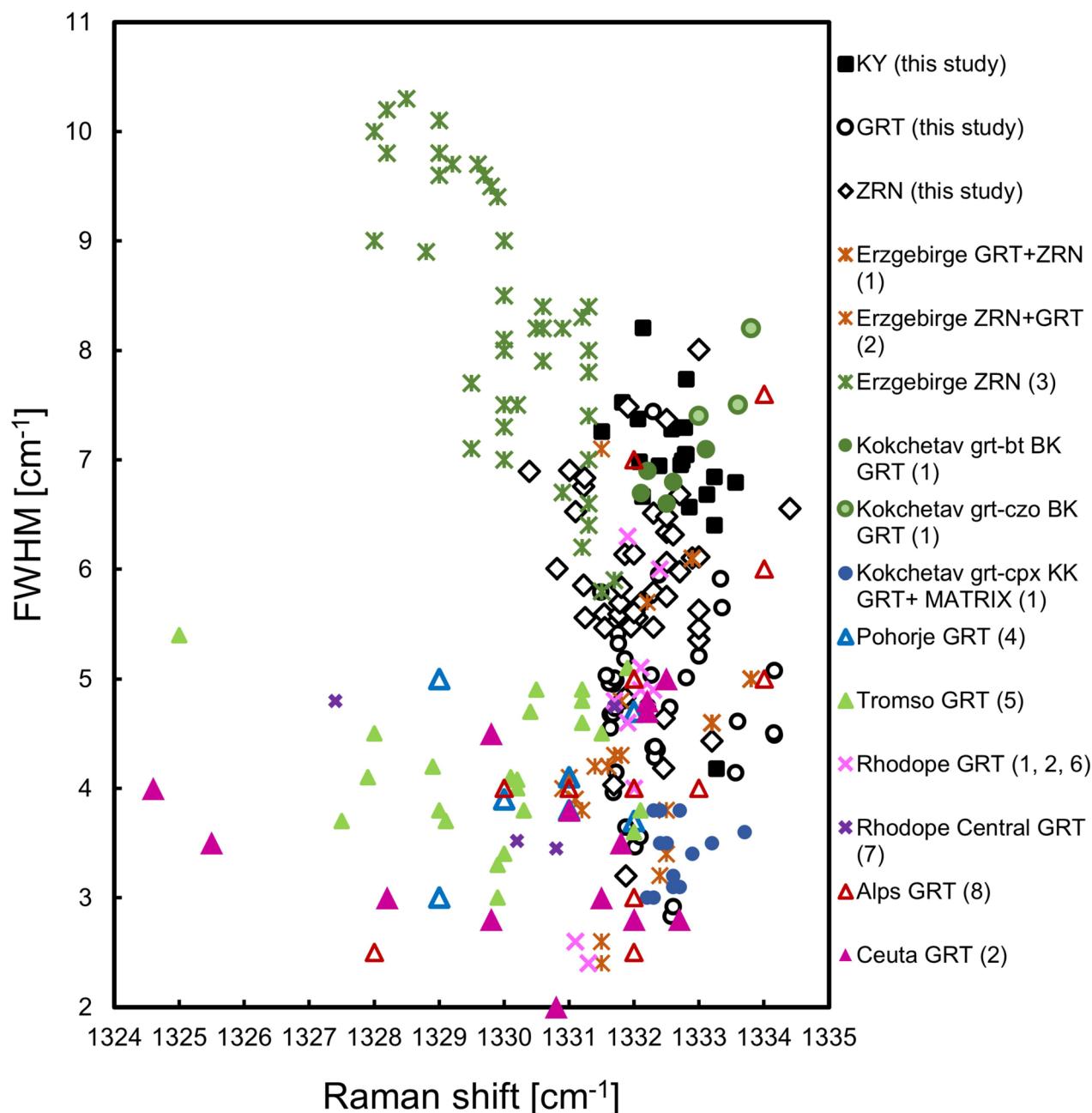


Fig. 6 – Raman data for microdiamonds worldwide compared to data from this study. Diamond inclusions in garnet (GRT), zircon (ZRN), in garnet-biotite rock (grt-bt), garnet-clinzoisite rock (grt-czo), garnet-clinopyroxene rock (grt-cpx), BK – Barchi Kol, Kokchetav Massif, KK – Kumdy Kol, Kokchetav Massif. References: 1 – Perraki et al. (2009), 2 – Nasdala et al. (2016), 3 – Zhang et al. (2017), 4 – Janák et al. (2015), 5 – Janák et al. (2013), 6 – Schmidt et al. (2010), 7 – Petřík et al. (2016), 8 – Frezzotti et al. (2011).

occur both individually and as a part of multiphase solid inclusion. The data show a broad negative correlation between the Raman shift and *FWHM*.

Microdiamonds in other HT–HP terranes (Perraki et al. 2009; Janák et al. 2013, 2015; Petřík et al. 2016), which commonly occur within polyphase inclusions enclosed in garnet, show no shift (Rhodope) but predominantly considerable downshift (Tromso, Pohorie, Ceuta), while their *FWHM* is relatively low (mostly > 2 to 3 cm⁻¹).

Diamonds from LT–HP rocks (Frezzotti et al. 2011), occurring in fluid inclusions, show no shift, upshift and downshift, and very variable *FWHM*.

4.2.3. Possible causes of variation of diamond Raman spectral parameters

Variations of Raman spectral parameters between diamonds and within individual diamond grains have been

commonly reported (e.g., Nasdala and Massone 2000; Zaitsev 2001; Perraki et al. 2009; Korsakov et al. 2015; Nasdala et al. 2016; Zhang et al. 2017). Below we consider the applicability of the earlier proposed causes of the deviations from the regular band position and width within the context of our data.

Some of the analyzed diamonds, namely those within kyanite, show the upshift and broadening of the Raman band. Moreover, the Raman maps of the elongated diamond grains from two different hosts (garnet and kyanite) revealed relative *FWHM* broadening in the cores compared to the rims, while the upshifted Raman bands show a relatively small and non-systematic change from core to rim. Our observation of the Raman shift variation of $\sim 1\text{cm}^{-1}$ within diamond grain is related to strain localization at edges, an effect measured and modeled by other authors (Campomenosi et al. 2018; Mazzucchelli et al. 2018). A similar distribution of the *FWHM* was reported by Korsakov et al. (2015) from an octahedral diamond grain enclosed in garnet in clinozoisite gneiss. These authors attributed the wider *FWHM* in the core to the imperfection of the diamond structure (cuboid evolving to octahedron, see discussion of morphology above). Crystal imperfections were also considered a cause for the *FWHM* broadening of the rapidly formed diamond, which was subject to shock metamorphism (Miyamoto et al. 1993). Neither two-phase growth nor such extreme conditions apply to our perfect octahedra, which reflects equilibrium growth (Kotková et al. 2021).

Nevertheless, we provide robust evidence for the presence of defects (dislocations) exclusively within these octahedral diamonds hosted by kyanite, which are, in our opinion, responsible for *FWHM* broadening. The formation of dislocations in diamond included in kyanite reflects the anisotropic thermal contraction of kyanite, possibly supported by its volume expansion during pressure release. On the other hand, the upshift observed in the case of inclusion in a stiffer host (e.g., garnet or zircon) is typically attributed to strain resulting in residual pressure inside the inclusion resulting from their different thermoelastic properties (see Perraki et al. 2009 and Nasdala et al. 2016 and references therein). This issue will be discussed in detail later.

Most of the diamonds in zircon (ZRN 95 and ZRN 95 SURF) and in garnet (GRT 95) show slight downshift or no shift accompanied by the Raman band broadening. Numerous explanations for the contemporaneous Raman band downshifting and *FWHM* increase were proposed: local heating by laser-light absorption, especially when the diamond is associated with graphite, tensile stress, nanometre size of a grain, the substitution of ^{13}C for ^{12}C , the incorporation of elevated levels of boron impurities, the internal stress variations caused by grain boundaries, or structural defects (see Perraki et al. 2009; Nasdala et

al. 2016 and references therein). Zhang et al. (2017) speculate about imperfect ordering due to rapid nucleation during short-term UHP metamorphism in the case of diamond hosted by zircon, without providing any evidence for this statement. In samples studied, the laser-induced upheating is disregarded due to the general absence of graphite, neither there is an effect of the nanometer size of all grains. Notably, the downshifting is in line with the elastic geobarometry theory (e.g., Rosenfeld and Chase 1961; Angel et al. 2015; see below).

Moderate Raman band broadening without any significant band shift can be attributed to nitrogen incorporation (Hanzawa et al. 1996; Surovtsev et al. 1999). Although nitrogen contents were not determined for the studied diamonds, the element is a common impurity in microdiamonds and its contents are variable (e.g., Sitnikova and Shatsky 2009). Thus, this explanation is possible.

The diamond grains exposed on the surface of zircon and garnet trend towards lower and higher wavenumbers relative to the encapsulated inclusions, respectively. Therefore, the upshift cannot be caused by the polishing, as reported for the polished diamond abrasives (Nasdala et al. 2016). This corroborates with Korsakov et al. (2015), who reported no measurable effect of polishing upon the Raman shift.

4.3. Elastic geobarometry

4.3.1. Theoretical background

Elastic geobarometry represents a method to determine peak P–T conditions of mineral formation, which is complementary to conventional geothermobarometry and phase equilibria. In contrast to the latter, elastic geobarometry uses mechanical equilibria controlled by mutual thermoelastic properties of inclusion and its host, and it is thus independent of chemical equilibrium between minerals (see, e.g., Kohn 2014; Angel et al. 2015; Moulas et al. 2020).

Simplified models assumed that the inclusion has to be small, individual, spherical, at the center of an infinite host, and that both phases are elastically isotropic or cubic and that there is no plastic deformation during the exhumation history (e.g., Zhang 1998; Angel et al. 2014, 2015). It needs to be mentioned, though, that recent models demonstrated that the errors imposed by the shape and size of the inclusion are lower than the uncertainty of the Raman measurement (Campomenosi et al. 2018; Mazzucchelli et al. 2019).

The presence of diamond inclusions in other phases not only provides evidence for the ultrahigh-pressure history of the rocks but moreover allows calculation of the P–T conditions when the inclusion was trapped (P_{trap}). At this point, the inclusion is elastically isolated

by the host, there is no significant stress neither in the host nor in the inclusion, both phases are at the same P–T condition, and their pressure is equal to the external pressure. Upon a change in P and T conditions, e.g. during the decompression, the change in volume of the host is different from that of the inclusion due to differences in their thermo-elastic properties, and non-lithostatic pressure develops in the inclusion as it is constrained by the host. This can be reflected by shifts in the characteristic Raman spectra (e.g., Izraeli et al. 1999).

To evaluate the entrapment pressure, we used the program EosFit-Pinc (Angel et al. 2017), which combines non-linear Equations of State (EoS) of the two phases with the calculation of the elastic relaxation, i.e., pressure change upon relaxation, which does not require an assumption of constant thermoelastic properties with geologically relevant changes of P and T (Angel et al. 2014). The program accounts for elastically isotropic spherical host-inclusion systems, represented in our case by diamond inclusions in garnet. It calculates the entrapment isomeke (Rosenfeld and Chase 1961), i.e., a line in P–T space defined by different thermodynamic properties of the two phases, along which the change in volume of host and inclusion is equal. The slope and curvature of an isomeke are controlled by the contrast of thermoelastic properties (thermal expansion coefficient, volume compressibility) of the inclusion and the host (Angel et al. 2015).

Elastic geobarometry has been commonly applied for a “soft” inclusion (e.g., garnet) in a “stiffer” host, e.g., diamond, where overpressure develops in the inclusion due to the relationship of their thermoelastic properties. In the case of a stiff (e.g., diamond) inclusion in a softer host (e.g., garnet), however, the situation is the opposite: the inclusion pressure is lower, as the diamond has relatively low thermal expansivity compared to its silicate host. Therefore, in the isomeke concept, the inclusion should develop under-pressure on exhumation (Angel et al. 2015).

Recent works showed that the concept of isomeke can also be used for the calculation of relaxation in the case that either host or inclusion has lower than cubic symmetry (e.g. Gonzalez et al. 2021). In the case of an isotropic diamond inclusion in an anisotropic host, such as kyanite and zircon, the anisotropic strain is developed in the host during the exhumation since the thermoelastic properties (thermal expansion and compressibility) differ along different axes.

4.3.2. Residual pressure estimates

Residual pressure (P_{inc}) has been measured using experimental data of Hanfland and Syassen (1985), who evaluated the effect of isotropic pressure on the frequency

of the first-order Raman mode of diamond at pressures between 15 GPa and 40 GPa. We have chosen their linear pressure coefficient of $2.9 \pm 0.05 \text{ cm}^{-1}/\text{GPa}$ because it is in close agreement with the low-pressure results reported in Mitra et al. (1969) and Whalley et al. (1976) under hydrostatic conditions up to 1.0 GPa and 2.3 GPa respectively. Tardieu et al. (1990) calculated a slightly different pressure coefficient of $2.64 \pm 0.10 \text{ cm}^{-1}/\text{GPa}$ based on experiments up to 14.5 GPa and a relatively low temperature of 400 °C. Their experiments confirmed that the change in the compressibility of the diamond as a function of T is very low. Nevertheless, our test showed that the use of both pressure coefficients provides comparable results. Based on the elastic theory, inclusions of the stiff diamond in a softer silicate host should show an underpressure. This holds true for the majority of diamonds enclosed in garnet and zircon ($P_{\text{inc}} \approx$ up to -0.14 ± 0.01 GPa in GRT 95 and -0.27 ± 0.01 GPa in ZRN 95 and up to -0.55 ± 0.01 GPa in ZRN 95 SURF) using the unstrained diamond standard as a reference.

An overpressure is observed in diamond both in acidic rock in kyanite (KY T7 0.13 ± 0.01 – 0.54 ± 0.01 GPa) and intermediate rock in garnet (GRT T38 0.07 ± 0.01 – 0.75 ± 0.01 GPa, GRT 95 SURF 0.19 ± 0.01 – 0.74 ± 0.01 GPa) and in zircon (ZRN St14 0.10 ± 0.01 – 0.83 ± 0.01 GPa); for more details see Supplementary data (ESM2).

By contrast, the highest value of overpressure (P_{inc}) 0.75 ± 0.01 GPa and 0.74 ± 0.01 GPa was calculated for the diamonds in GRT T38 and GRT 95 SURF, respectively.

The measured overpressure in diamonds (GRT T38) may reflect the conditions of elastic resetting of inclusion under conditions different from the original entrapment, i.e., at high temperature and lower pressure, which is consistent with the adiabatic exhumation P–T path reconstructed for the UHP rock based on thermodynamic modeling (Haifler and Kotková 2016). This could happen by the plastic deformation of the host (Angel et al. 2015; Ferrero and Angel 2018).

In our case, we observe overpressure in diamonds on the surface of the same rock sample (95 SURF), where the diamonds underneath the surface show an underpressure (95). At the same time, the over-pressured diamonds in sample T38 occur in a cluster and close to each other, and several diamonds in T38 enclosed within a single garnet domain show a range of Raman shift from upshift to downshift. These variations in closely associated diamonds cannot be attributed to chemical variability of the host garnet as suggested, e.g., by Campomenosi et al. (2018) or Mazzucchelli et al. (2018). Similarly, the overpressure cannot be related to diamond transformation to graphite (Ferrero and Angel 2018), as this has not been observed in the studied samples and the (late) graphite occurrence is very restricted. The observed variability of

the inclusion pressure would imply a variable degree of elastic resetting of diamonds located in the same garnet domain along the decompression path.

The overpressure in diamond GRT T38 can be related to the occurrence of diamonds in clusters, or at least close to each other, which is a common feature in the intermediate rocks. However, such a situation does not meet the requirements for the use of elastic geobarometry. Diamonds with variable morphology exposed on the surface (GRT 95 SURF) show different values of Raman band shift and calculated P_{inc} in the range of -0.18 ± 0.1 – 0.74 ± 0.1 GPa. The underpressure was detected in cuboid diamond with graphite on the interface with garnet and growth dislocations in the interior (Figs 2h, 3d–e). Imperfect polycrystalline diamond (Fig. 3f) shows an overpressure of 0.47 ± 0.1 GPa. This diamond morphology examination (TEM, SEM) altogether with measured Raman spectral parameters significantly contributes to knowledge of diamond character variability and thus possible variability in Raman band shift and $FWHM$ within GRT 95 SURF. Such variability in, e.g., possible polycrystalline character or gap or presence of associated phases is also expected for diamonds underneath the surface.

4.3.3. Entrapment pressure estimates

The calculated values of under- and over-pressure in diamond in garnet 95 were subsequently used to determine the pressure of the inclusion entrapment using the program EosFit-Pinc (Angel et al. 2017) with Mie-Grüneisen-Debye EoS (Angel et al. 2022) for a garnet host with the chemical composition of $X_{Grs}=0.3$ $X_{Prp}=0.3$ and $X_{Alm}=0.4$, and the peak temperatures of 1100°C (Haifler and Kotková 2016). Next, we focused on calculating P_{trap} from the system diamond (inclusion) – garnet 95 (host) to test the reliability of elastic geothermobarometry for the sample 95, where the peak P–T of ca. 4.5–5.0 GPa and $\geq 1100^\circ\text{C}$ and isothermal decompression P–T path were constrained using conventional thermobarometry and thermodynamic modeling (Haifler and Kotková 2016).

The mean entrapment pressure P_{trap} calculated from entrapment pressures for each diamond grain in GRT 95 corresponds to 4.81 ± 0.14 GPa and 4.99 ± 0.14 GPa using a standard diamond from literature and unstrained diamond during the measurement, respectively, as a reference (ESM1 and 2). Both results are comparable and within the earlier estimate by Haifler and Kotková (2016) (Fig. 7).

4.3.4. Stress distribution

The Raman maps of two non-spherical grains (elongated diamond in garnet GRT T38) and octahedral grain in

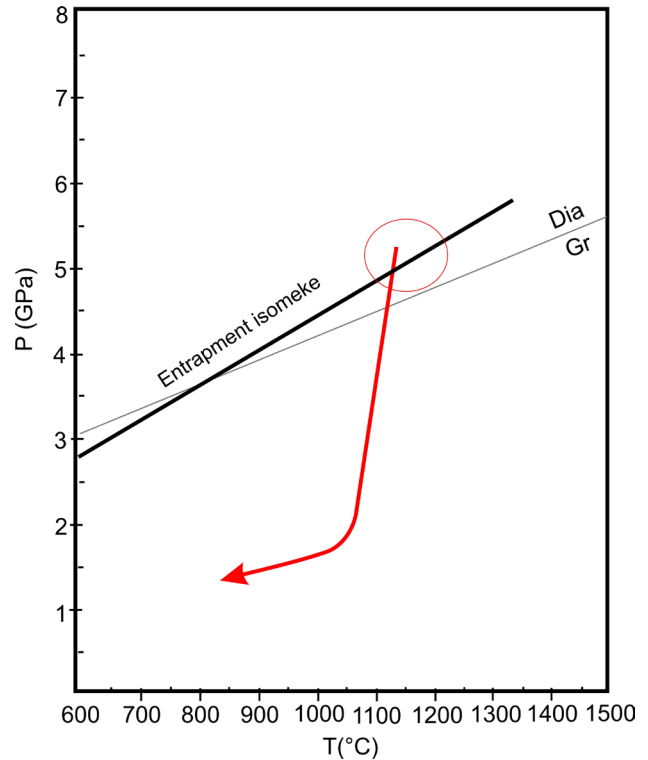


Fig. 7 – The entrapment isomeke and the peak pressure estimated for diamond-in-garnet 95 (circle). Exhumation P–T path from Haifler and Kotková (2016) is also shown. Graphite/diamond transition curve from Day (2012)

kyanite (KY T7) show small non-systematic variations in Raman up-shifted bands. According to the theory of elasticity, faceted inclusion exhibits a non-homogenous Raman shift opposite to the rounded one (Campomenosi et al. 2018; in line with Mazzuchelli et al. 2018; Eshelby 1957). Heterogeneity in Raman shift and the presence of overpressure can be related to the presence of edges and corners, which act as stress concentrators (Campomenosi et al. 2018; Murri et al. 2018). Moreover, the grain in garnet is closely associated with another diamond grain and does not meet the requirement of sole inclusion in a host.

5. Conclusions

Here we present the results of a study of Raman spectral parameters of microdiamonds combined with data on their morphology, internal structure, and relationship to their host.

1. We suggest that the octahedron represents the initial growth form of cuboctahedra in UHP terranes, which challenges the existing model. We further argue that the evolution from octahedra to cuboctahedra reflects rather cooling than increasing supersaturation of the crystallizing medium.
2. The combined data for diamonds show that the upshift of the Raman band, translated into the overpressure, is

characteristic of diamonds enclosed in kyanite, and is consistent with the closed interface. We suggest that dislocations observed exclusively in these diamonds are responsible for the high observed *FWHM*.

3. Diamonds enclosed in garnet and zircon exhibit higher variation in their Raman spectral parameters, reflecting their complex internal features and the presence of other phases. These diamonds show mostly downshift or no shift, in line with the elastic barometry theory and consistent with the open diamond-host interface.
4. The calculated entrapment pressure for a diamond in garnet 95, exhibiting downshift, corresponds to 4.81 ± 0.14 – 4.99 ± 0.14 GPa at an entrapment temperature of 1100 °C, which is consistent with earlier estimates and does not require any elastic resetting neither plastic deformation. The upshift/overpressure observed in some cases can be related to the proximity of other diamond grains, which does not meet the requirements of the elastic geobarometry. The overpressure cannot be explained by the formation of graphite coating on diamond.
5. The Raman shift variation of ~ 1 cm⁻¹ within diamond grains from Raman mapping relates to the faceted character of the inclusions resulting in a non-homogeneous Raman shift.
6. Both upshift and downshift measured in diamonds on the surface exclude the effect of polishing on the diamond Raman spectral parameters.

We conclude that the use of diamond in elastic barometry requires knowledge of its internal structure and presence of associated phases and should be restricted to isometric monocrystalline diamond grains not occurring in clusters.

Acknowledgments. This research was financially supported by the institutional research fund of the Faculty of Science, Masaryk University (1344/315010) to PJ and represents a contribution to the Strategic Research Plan of the Czech Geological Survey (DKRVO/ČGS 2018-2022, JK). We acknowledge discussions with Y. Fedortchouk concerning diamond morphology, and constructive comments of M. Janák, M. Perraki, M. Cisneros and an anonymous reviewer that improved the manuscript significantly. R. Skála is thanked for careful and efficient editorial handling, same as the Editor-in-chief.

Electronic supplementary material. Supplementary material are available online on the Journal website (<http://dx.doi.org/10.3190/jgeosci.356>).

References

ANGEL RJ, MAZZUCHELLI ML, ALVARO M, NIMIS P, NESTOLA F (2014) Geobarometry from host-inclusion

systems: The role of elastic relaxation. *Amer Miner* 99: 2146–2149

ANGEL RJ, NIMIS P, MAZZUCHELLI ML, ALVARO M, NESTOLA F (2015) How large are departures from lithostatic pressure? Constraints from host-inclusion elasticity. *J Metamorph Geol* 33: 801–813

ANGEL RJ, MAZZUCHELLI ML, ALVARO M, NESTOLA F (2017) EosFit-Pinc: A simple GUI for host-inclusion elastic thermobarometry. *Amer Miner* 102: 1957–1960

ANGEL RJ, MURRI M, MIHAILOVA B, ALVARO M (2018) Stress, strain and Raman shifts, EosFit-Pinc: A simple GUI for host-inclusion elastic thermobarometry. *Z Kristallogr* 234(2): 129–140

ANGEL RJ, GILLIO M, MAZZUCHELLI M, ALVARO M (2022) Garnet EoS: a critical review and synthesis. *Contrib Mineral Petrol* 177:54 DOI 10.1007/s00410-022-01918-5

BARNARD AS (2013) Diamond nanoparticles as a new platform for the sequestration of waste carbon. *Phys Chem Chem Phys* 23: 9156–9162

BONAZZI M, TUMIATI S, THOMAS JB, ANGEL RJ, ALVARO M (2019) Assessment of the reliability of elastic geobarometry with quartz inclusions. *Lithos* 350–351: 105201

BOVENKERK HP (1961) Some observations on the morphology and physical characteristics of synthetic diamond. *Amer Miner* 46: 952–963

CAMPOMENOSI N, MAZZUCHELLI ML, MIHAILOVA BD, SCAMBELLURI M, ANGEL RJ, NESTOLA F, REALI A, ALVARO M (2018) How geometry and anisotropy affect residual strain in host inclusion systems: coupling experimental and numerical approaches. *Amer Miner* 103: 2032–2035

CHERNOV AA (1974) Stability of faceted shapes. *J Cryst Growth* 24/25: 11–31

DAY HW (2012) A revised diamond–graphite transition curve. *Amer Miner* 97: 52–62

DE CORTE K, KORSKOV A, TAYLOR WR, CARTIGNY P, ADER M, DE PAEPE P (2000) Diamond growth during ultrahigh-pressure metamorphism of the Kokchetav Massif, northern Kazakhstan. *Isl Arc* 9: 428–438

DOBZHINETSAYA LF, GREEN HW, MITCHELL TE, DICKERSON RM (2001) Metamorphic diamonds: Mechanism of growth and inclusion of oxides. *Geology* 29: 263–266

DOBZHINETSAYA LF, GREEN HW, BOZHILOV KN, MITCHELL TE, DICKERSON RM (2003) Crystallization environment of Kazakhstan microdiamond: evidence from nanometric inclusion and mineral associations. *J Metamorph Geol* 21: 425–437

DOBZHINETSAYA LF, WIRTH R, GREEN HW (2007) A look inside of diamond-forming media in deep subduction zones. *Proc Natl Acad Sci USA* 104: 9128–9132

DOBZHINETSAYA LF (2012) Microdiamonds – Frontiers of ultrahigh-pressure metamorphism: A review. *Gondwana Res* 21: 207–223

- DOBZHINETSAYA LF, WIRTH R, GREEN HW, SCHREIBER A, OBANNON E (2013) First find of polycrystalline diamond in ultrahigh-pressure metamorphic terrane of Erzgebirge, Germany. *J Metamorph Geol* 31: 5–18
- ENAMI M, NISHIYAMA T, MOURI T (2007) Laser Raman microspectrometry of metamorphic quartz: a simple method for comparison of metamorphic pressures. *Amer Miner* 92: 1303–1315
- ESHELBY JD (1957) The determination of the elastic field of an ellipsoidal inclusion, and related problems. *Proc R Soc Lond* 241: 376–396
- FERRERO S, ANGEL RJ (2018) Micropetrology: are inclusions grains of truth? *J Petrol* 59: 1671–1700
- FREZZOTTI ML, SELVERSTONE J, SHARP ZD, COMPAGNONI R (2011) Carbonate dissolution during subduction revealed by diamond-bearing rocks from the Alps. *Nat Geosci* 4: 703–706
- GOLDSCHMIDT V (1916) *Atlas der Krystallformen*, Vol. 3. *Diamant Tafeln*. Carl Winters Universitätsbuchhandlung, Heidelberg
- GONZALEZ JP, MAZZUCHELLI ML, ANGEL RJ, ALVARO M (2021) Elastic geobarometry for anisotropic inclusions in anisotropic host minerals: quartz-in-zircon. *J Geophys Res Solid Earth* DOI 10.1029/2021JB022080
- GURNEY JJ, HILDEBRAND PR, CARLSON JA, FEDORTCHOUK Y, DYCK DR (2004) The morphological characteristics of diamonds from the Ekati property, Northwest Territories, Canada. *Lithos* 77: 21–38
- HAIFLER J, KOTKOVÁ J (2016) UHP-UHT peak conditions and near-adiabatic exhumation path of diamond-bearing garnet–clinopyroxene rocks from the Eger Crystalline Complex, North Bohemian Massif. *Lithos* 248: 366–381
- HANFLAND M, SYASSEN K (1985) Pressure dependence of the first-order Raman mode in diamond. *Phys Rev B* 31: 6896–1899
- HANZAWA H, UMEMURA N, NISIDA Y, KANDA H, OKADA M, KOBAYASHI M (1996) Disorder effects of nitrogen impurities, irradiation-induced defects, and ^{13}C isotope composition on the Raman spectrum in synthetic Ib diamond. *Phys Rev B* 54: 3793–3799
- IZRAELI ES, HARRIS JW, NAVON O (1999) Raman barometry of diamond formation. *Earth Planet Sci Lett* 173: 351–360
- JANÁK M, KROGH RAVNA EJK, KULLERUD K, YOSHIDA K, MILOVSKÝ R, HIRAJIMA T (2013) Discovery of diamond in the Tromsø Nappe, Scandinavian Caledonides (N. Norway). *J Metamorph Geol* 31: 691–703
- JANÁK M, FROITZHEIM N, YOSHIDA Y, SASINKOVÁ V, NOSKO M, KOBAYASHI T, HIRAJIMA T, VRABEC M (2015) Diamond in metasedimentary crustal rocks from Pohorje, Eastern Alps: a window to deep continental subduction. *J Metamorph Geol* 33: 495–512
- KNIGHT DS, WHITE WB (1989) Characterization of diamond films by Raman spectroscopy. *J Mater Res* 4: 385–393
- KOHN MJ (2014) “Thermoba-Raman-try”: calibration of spectroscopic barometers and thermometers for mineral inclusions. *Earth Planet Sci Lett* 388: 187–196
- KORSAKOV AV, SHATSKY VS, SOBOLEV NV, ZAYACHOKOVSKY AA (2002) Garnet-biotite-clinozoisite gneiss: a new type of diamondiferous metamorphic rock from the Kokchetav Massif. *Eur J Mineral* 14: 915–928
- KORSAKOV AV, VANDENABEELE P, THEUNISSEN K (2005) Discrimination of metamorphic diamond populations by Raman spectroscopy (Kokchetav, Kazakhstan). *Spectrochim Acta A* 61: 2378–2385
- KORSAKOV AV, PERRAKI M, ZEDGENIZOV D, BINDI L, VANDENABEELE P, SUZUKI A, KAGI H (2010) Diamond-Graphite Relationships in Ultrahigh-pressure Metamorphic Rocks from the Kokchetav Massif, Northern Kazakhstan. *J Petrol* 51: 763–783
- KORSAKOV AV, TOPORSKI J, DIEING T, YANG J, ZELENOSKIY Ps (2015) Internal diamond morphology: Raman imaging of metamorphic diamonds. *J Raman Spectrosc* 46: 880–888
- KOTKOVÁ J (1993) Tectonometamorphic history of lower crust in the Bohemian Massif – example of north Bohemian granulites. *Spec Pap Czech Geol Survey* 2: pp 1–42
- KOTKOVÁ J, KRÖNER A, TODT W, FIALA J (1996) Zircon dating of North Bohemian granulites, Czech Republic: further evidence for the lower carboniferous high-pressure event in the Bohemian Massif. *Geol Rundsch* 85: 154–161
- KOTKOVÁ J, O’BRIEN PJ, ZIEMANN MA (2011) Diamond and coesite discovered in Saxony-type granulite: solution to the Variscan garnet peridotite enigma. *Geology* 39: 667–670
- KOTKOVÁ J, WHITEHOUSE M, SCHALTEGGER U, D’ABZAC FX (2016) The fate of zircon during UHT–UHP metamorphism: isotopic (U/Pb, ^{18}O , Hf) and trace element constraints. *J Metamorph Geol* 34: 719–739
- KOTKOVÁ J, FEDORTCHOUK Y, WIRTH R, WHITEHOUSE MJ (2021) Metamorphic diamonds formation is controlled by water activity phase transitions and temperature. *Sci Rep* 11:7694
- KRISHNAMURTI D (1954) The Raman spectrum of diamond. *Proc Indian Acad Sci A* 40: 211–216
- MAZZUCHELLI ML, BURNLEY P, ANGEL RJ, MORGANTI S, DOMENEGHETTI MC, NESTOLA F, ALVARO M (2018) Elastic geothermobarometry: Corrections for the geometry of the host-inclusion system. *Geology* 46: 231–234
- MAZZUCHELLI ML, REALI A, MORGANTI S, ANGEL RJ, ALVARO M (2019) Elastic geobarometry for anisotropic inclusions in cubic hosts. *Lithos* 350–351: 105218
- MEDARIS LG, ACKERMAN L, JELÍNEK E, ZACHARY DM, ERBAN V, KOTKOVÁ J (2015) Depletion, cryptic metasomatism, and modal mesomatism (refertilization) of Variscan lithospheric mantle: evidence from major

- elements, trace elements, and Sr–Nd–Os isotopes in a Saxothuringian garnet peridotite. *Lithos* 226: 81–97
- MIYAMOTO M, TAKASE T, MITSUDA Y (1993) Raman spectra of various diamonds. *Mineral J* 16: 246–257
- MITRA SS, BRAFMAN O, DANIELS WB, CRAWFORD RK (1969) Pressure-induced phonon frequency shifts measured by Raman scattering. *Phys Rev* 186: 942–944
- MOULAS E, KOSTOPOULOS D, PODLADCHIKOV Y, CHATZITHEODORIDIS E, SCHENKER FE, ZINGERMAN KM, PANAGIOTIS P, TAJČMANOVÁ L (2020) Calculating pressure with elastic geobarometry: A comparison of different elastic solutions with application to a calc-silicate gneiss from the Rhodope Metamorphic Province. *Lithos*: 378–379, 105803
- MURRI M, MAZZUCHELLI ML, CAMPOMENOSI N, KORSAKOV AV, PRENCIPE M, MIHAILOVA BD, SCAMBELLURI M, ANGEL RJ, ALVARO M (2018) Raman elastic geobarometry for anisotropic mineral inclusions. *Amer Miner* 103: 1869–1872
- NASDALA L, STEGER S, REISSNER C (2016) Raman study of diamond-based abrasives, and possible artefacts in detecting UHP microdiamond. *Lithos* 265: 317–327
- NASDALA L, MASSONNE HJ (2000) Microdiamonds from the Saxonian Erzgebirge, Germany: in situ micro-Raman characterisation. *Eur J Mineral* 12: 495–498
- OGASAWARA Y (2005) Microdiamonds in ultrahigh-pressure metamorphic rocks. *Elements* 1: 91–96
- PARKINSON CD, KATAYAMA I (1999) Present-day ultrahigh-pressure conditions of coesite inclusion in zircon and garnet: Evidence from laser Raman microspectroscopy. *Geology* 27: 979–982
- PETRÍK I, JANÁK M, FROITZHEIM N, GEORGIEV N, YOSHIDA K, SASINKOVÁ V, KONEČNÝ P, MILOVSKÁ S (2016) Triassic to Early Jurassic (c. 200 Ma) UHP metamorphism in the Central Rhodopes: evidence from U–Pb–Th dating of monazite in diamond-bearing gneiss from Chepelare (Bulgaria). *J Metamorph Geol* 34: 265–291
- PERRAKI M, KORSAKOV AV, SMITH DC, MPOSKOS E (2009) Raman spectroscopic and microscopic criteria for the distinction of microdiamonds in ultrahigh-pressure metamorphic rocks from diamonds in sample preparation materials. *Amer Miner* 94: 546–556
- ROSENFELD JL, CHASE AB (1961) Pressure and temperature of crystallization from elastic effects around solid inclusion minerals? *Am J Sci* 259: 519–541
- SCHMIDT S, NAGEL TJ, FROITZHEIM N (2010) A new occurrence of microdiamond-bearing metamorphic rocks, SW Rhodopes, Greece. *Eur J Mineral* 22: 189–198
- SHATSKY VS, RYLOV GM, EFIMOVA ES, DE CORTE K, SOBOLEV NV (1998) Morphology and real structure of microdiamonds from metamorphic rocks (Kokchetav Massif), kimberlites, and alluvial placers. *Russ Geol Geophys* 39: 949–961
- SITNIKOVA ES, SHATSKY VS (2009) New FTIR spectroscopy data on the composition of the medium of diamond crystallization in metamorphic rocks of the Kokchetav Massif. *Russ Geol Geophys* 50: 842–849
- SMITH DC, GODARD G (2013) A Raman spectroscopic study of diamond and disordered sp³-carbon in the coesite-bearing Straumen Eclogite Pod, Norway. *J Metamorph Geol* 31: 19–33
- SOLIN SA, RAMDAS AK (1970) Raman spectrum of diamond. *Phys Rev B* 1: 1687–1698
- STÖCKHERT B, DUYSER J, TREPMANN C, MASSONNE HJ (2001) Microdiamond daughter crystals precipitated from supercritical COH plus silicate fluids included in garnet, Erzgebirge, Germany. *J Metamorph Geol* 27: 673–684
- STÖCKHERT B, TREPMANN CA, MASSONNE HJ (2009) Decrepitated UHP fluid inclusions: about diverse phase assemblages and extreme decompression rates (Erzgebirge, Germany). *Geology* 29: 391–394
- SUNAGAWA I. (2005) Crystals – Growth, Morphology and Perfection. Cambridge University Press, Cambridge, New York, Melbourne, pp 1–295
- SUROVTSEV NV, KUPRIYANOV IN, MALINOVSKY VK, GUSEVA VA, PALYANOV YN (1999) Effect of nitrogen impurities on the Raman line width in diamonds. *J Phys Condens Matter* 11: 4767–4774
- TARDIEU A, CANSELL F, PETITET JP (1990) Pressure and temperature dependence of the first-order Raman mode of diamond. *J Appl Phys* 68: 3243–3245
- VÁČZI T (2014). A new, simple approximation for the deconvolution of instrumental broadening in spectroscopic band profiles. *Appl Spectrosc* 68: 1274–1278
- WARR LN (2021) IMA–CNMNC approved mineral symbols. *Mineral Mag* 85: 291–320
- WHALLEY E, LAVERGNE A, WONG PTT (1976) Hydrostatic optical cell with glass windows for 25 kbar. *Rev Sci Instrum* 47: 845–848
- WIRTH R (2004) Focused ion beam (FIB); a novel technology for advanced application of micro- and nanoanalysis in geo-sciences and applied mineralogy. *Eur J Mineral* 16: 863–876
- WIRTH R, GERDES A, KEMP AIS, HANCHAR JM, SCHERSTEN A (2009) Focused ion beam (FIB) combined with SEM and TEM; advanced analytical tools for studies of chemical composition, microstructure and crystal structure in geomaterials on a nanometre scale. *Chem Geol* 261: 217–229
- WOODRUFF DP (2015) How does your crystal grow? A commentary on Burton, Cabrera and Frank (1951) ‘The growth of crystals and the equilibrium structure of their surfaces’. *Phil Trans R Soc A* 373: 20140230
- YAMAOKA S, KOMATSU H, KANDA H, SETAKA N (1977) Growth of diamond with rhombic dodecahedral faces. *J Cryst Growth* 37: 349–352
- YU X, RATERRON P, ZHANG J, LIN Z, WANG L, ZHAO Y (2012): Constitutive law and flow mechanism in diamond deformation. *Sci Rep* 2: 876

- ZAITSEV AM (2001) *Optical Properties of Diamond*. Springer, New York, pp 502
- ZHANG Y (1998) Mechanical and phase equilibria in inclusion–host systems. *Earth Planet Sci Lett* 157: 209–222
- ZHANG RU, LIOU JG, CHING-HUA L (2017) Raman spectra of polycrystalline microdiamond inclusions in zircons, and ultrahigh-pressure metamorphism of a quartzofeldspathic rock from the Erzgebirge terrane, Germany. *Int Geol Rev* 59: 779–792
- ZHONG X, MOULAS E, TAJČMANOVÁ L (2018) Tiny timekeepers witnessing high-rate exhumation processes. *Sci Rep* 8: 2234, DOI 10.1038/s41598-018-20291-7